Original Article

Detecting bone marrow infiltration in nonosteolytic multiple myeloma through separation of hydroxyapatite via the two-material decomposition technique in spectral computed tomography

Jianhua Chen[1]^, Zongjian Qiu[2]^, Nan Jiang[1]^, Yu Xia[1]^, Hongxiang Li[1]^, Suping Chen[3]^, Jianfang Liu[1]^, Yunjing Xue[1]^

[1]Department of Radiology, Fujian Medical University Union Hospital, Fuzhou, China; [2]Fujian Institute of Hematology, Fujian Provincial Key Laboratory on Hematology, Fujian Medical University Union Hospital, Fuzhou, China; [3]GE HealthCare, Beijing, China

Contributions: (I) Conception and design: J Chen, J Liu, Y Xue; (II) Administrative support: J Liu, Y Xue; (III) Provision of study materials or patients: Z Qiu, N Jiang, Y Xia; (IV) Collection and assembly of data: Z Qiu, N Jiang, Y Xia, H Li; (V) Data analysis and interpretation: J Chen, H Li, S Chen, J Liu, Y Xue; (VI) Manuscript writing: All authors; (VII) Final approval of manuscript: All authors.

Correspondence to: Jianfang Liu, MD; Yunjing Xue, MD. Department of Radiology, Fujian Medical University Union Hospital, 29 Xinquan Road, Gulou District, Fuzhou 350001, China. Email: liujianfang1210@163.com; xueyunjing@126.com.

Background: Conventional computed tomography (CT) has low sensitivity for the diagnosis of bone marrow infiltration in nonosteolytic multiple myeloma (NOL-MM). This study aimed to compare the performance of the two-material decomposition technique of spectral CT with the removal of X-ray absorption components of calcium (Ca) versus that of hydroxyapatite (HAP) for diagnosis of NOL-MM.

Methods: From October 2022 to March 2023, a total of 41 consecutive patients with MM without focal bone lesions undergoing chest spectral CT and thoracic spine magnetic resonance imaging (MRI) in Fujian Medical University Union Hospital were prospectively enrolled; meanwhile, another set of 41 age- and sex-matched healthy consecutive participants were selected as a comparison group. Based on MRI findings, patients with MM were classified with a diffuse infiltration pattern MM (DP-MM) or a normal pattern MM (NP-MM). Regions of interest (ROIs) were manually drawn on vertebrae. CT values of 70-keV images and basic material density within the ROIs were stored. The basic two-material pairs included a Ca-related pair (Ca-X) and an HAP-related pair (HAP-X), with *X* referring to fat, water, or muscle. Material density values $D_{Ca(X)}$, $D_{X(Ca)}$, $D_{HAP(X)}$, and $D_{X(HAP)}$ were each used to diagnose MM, and the area under the receiver operating characteristic curve (AUC) was used to assess diagnostic performance.

Results: The 41 patients with NOL-MM included 30 with DP-MM and 11 with NP-MM. CT value, $D_{Ca(X)}$, and $D_{HAP(X)}$ were comparable between the NOL-MM, DP-MM, NP-MM, and comparison groups. $D_{X(HAP)}$ was better than $D_{X(Ca)}$ for distinguishing the NOL-MM group from the comparison group {AUC [95% confidence interval (CI)], 0.874 (0.800, 0.949) *vs.* 0.737 (0.630, 0.844); P=0.02}, the DP-MM group from the comparison group [AUC (95% CI), 0.933 (0.878, 0.989) *vs.* 0.785 (0.677, 0.894); P=0.01], the NP-MM group from the comparison group [AUC (95% CI), 0.714 (0.540, 0.888) *vs.* 0.605 (0.429, 0.782); P=0.03], and the DP-MM group from the NP-MM group [AUC (95% CI), 0.809 (0.654, 0.964) *vs.* 0.736 (0.566, 0.907); P=0.049]. The diagnostic performance of $D_{X(HAP)}$ and $D_{X(Ca)}$ was influenced only by the removed

^ ORCID: Jianhua Chen, 0009-0002-2575-7803; Zongjian Qiu, 0009-0007-3298-2714; Nan Jiang, 0009-0001-2138-0300; Yu Xia, 0009-0008-7245-0058; Hongxiang Li, 0000-0003-2346-9592; Suping Chen, 0009-0004-3522-9291; Jianfang Liu, 0000-0002-9235-3166; Yunjing Xue, 0000-0003-4563-4763.

material, while the X material had no influence.

Conclusions: The spectral CT two-material decomposition technique with removal of X-ray absorption components of HAP is useful for diagnosis of NOL-MM, irrespective of the paired material.

Keywords: Multiple myeloma (MM); dual-energy computed tomography (dual-energy CT); hydroxyapatite (HAP); bone marrow infiltration

Submitted Jul 21, 2023. Accepted for publication Jan 11, 2024. Published online Mar 04, 2024.
doi: 10.21037/qims-23-1042
View this article at: https://dx.doi.org/10.21037/qims-23-1042

Introduction

Multiple myeloma (MM) is the second most common hematological malignancy. It is characterized by unrestricted clonal proliferation of plasma cells, which can lead to osteolytic bone destruction if the bone marrow is involved (1). Bone disease is the most common manifestation of MM and the main cause of MM-associated mortality and morbidity. Computed tomography (CT) is the preferred method for diagnosing MM osteolytic lesions, but nonosteolytic (NOL) bone marrow infiltration may appear normal or as osteoporosis on CT and so is often underestimated (1). Magnetic resonance imaging (MRI), with its superior soft tissue contrast, can detect bone marrow infiltration even before bone destruction occurs and is therefore the gold standard for the diagnosis of bone marrow infiltration (2). However, MRI is expensive and time-consuming, with many contraindications, thus limiting its use in clinical practice.

The low sensitivity of conventional CT for diagnosis of NOL lesions is mainly due to the influence of dense bone trabeculae (3). If the influence of bone trabeculae can be removed or reduced, CT detection of NOL bone marrow infiltration might be improved. The development of dual-energy CT (DECT) has brought new opportunities for the diagnosis of nonosteolytic multiple myeloma (NOL-MM) bone marrow infiltration. X-ray photons are not only attenuated differently by different substances but also at different energies, which makes DECT possible. The linear attenuation coefficient of a specific material is a function of energy, causing the material to behave differently at different X-ray spectra. In DECT, two spectra are employed to reconstruct material decomposition maps, simulating the linear attenuation coefficient as a function of energy. The DECT method was first proposed by Alvarez and Macovski in 1976 and later on, the Hasegawa group implemented the first practical DECT system (4-7). The primary advantage of DECT is conservation of the energy-dependent interactions. This advantage provides invaluable insights for determining the effective atomic number for the accurate assessment of the chemical composition contributions and the mass density to the CT number through material decomposition of typically two or three basis materials. Material-specific images [e.g. calcium (Ca) and hydroxyapatite (HAP)] can be created with material decomposition; conversely, materials can be suppressed to generate virtual noncontrast images (8).

With the advancement of CT hardware and software technology, several DECT methods have become available, with the main methods for obtaining dual-energy being the dual-source (Siemens HealthCare) and rapid kilovoltage switching (GE HealthCare) techniques (hereinafter referred to as spectral CT), among others (9). Most dual-source protocols found in MM studies involve three-material decomposition in the image-space domain; separating bone into Ca, red marrow, and yellow marrow; and subtracting the contribution of Ca from the data set to generate a virtual non-Ca image. Meanwhile, two-material decomposition uses the absorption characteristics of two basic paired materials (e.g., fat and Ca or water and Ca) with different effective atomic numbers and mass-attenuation coefficients to obtain two sets of images (commonly referred to as material density images) (10). These material density images are obtained by selective segmentation and separation of paired basic materials to produce single-material density images without the X-ray absorption components related to the paired material. For example, when a basic fat-Ca pair is used, the fat (Ca) density image and the Ca (Fat) density image will be obtained separately: the former is a fat absorption image obtained by removing Ca absorption components, while the latter is a Ca absorption image obtained by removing the fat absorption components (10).

Most studies on methods for removing the influence

of trabecular bone to improve observation of MM bone marrow lesions have been related to three-material decomposition of dual-source CT, and studies on two-material decomposition of spectral CT are rare (11). Dual-source CT uses three-material decomposition to subtract Ca from images and highlight anatomical structures covered with bone mineral or gross calcifications, but HAP is also a major inorganic component of bone (12). This study thus aimed to compare the performance of the two-material decomposition technique in spectral CT for diagnosing NOL-MM by removing Ca versus HAP, both major components of bone trabeculae. We present this article in accordance with the STARD reporting checklist (available at https://qims.amegroups.com/article/view/10.21037/qims-23-1042/rc).

Methods

Ethical statement

This prospective, single-center study was conducted in accordance with the Declaration of Helsinki (as revised in 2013) and was approved by the institutional ethics board of Fujian Medical University Union Hospital. Informed consent was obtained from all participants.

Patients

This study was conducted at Fujian Medical University Union Hospital. A total of 41 patients diagnosed with MM between October 2022 and March 2023 were consecutively included only if they met all of the following criteria: (I) admission to hospital was based increased serum levels of abnormal monoclonal accessory proteins (>30 g/L); (II) the diagnosis of MM was based on the updated International Myeloma Working Group diagnostic criteria (13); and (III) whole-spine MRI [including T1-weighted imaging (T1WI) and short tau inversion recovery (STIR) sequences] and chest spectral CT evaluations were conducted, with an interval of ≤2 weeks between the two examinations. The exclusion criteria were the following: (I) an inability to complete MRI examination, (II) a history of malignant tumors other than MM, (III) a history of spinal trauma, (IV) obvious focal osteolytic lesions on CT (as identified by two radiologists, reader 1 and reader 2, each with 9–11 years of experience in musculoskeletal imaging diagnosis and disagreements being resolved by discussion), and (V) poor image quality.

Another set of 41 age- and sex-matched participants who underwent the same imaging protocol for annual follow-up of lung nodules were consecutively selected to form a comparison group.

Spectral CT scanning protocol

The Revolution CT scanner (GE HealthCare, Chicago, IL, USA) was used to perform examinations on all patients, and the Gemstone Spectral Imaging (GE HealthCare) mode was used for nonenhanced scans, covering the chest from the lung apex to the adrenal gland. The parameters were as follows: tube voltages of 80 and 140 kV (instantaneous switching), spectral CT adaptive current, a slice thickness of 5 mm, layer spacing of 1 mm, a pitch of 1.375, and a volume CT dose index of 10.30 mGy. For axial images, 70-keV images were reconstructed with a slice thickness of 1.25 mm. The scanner was calibrated before the study, and daily quality comparison scans were performed during the study to confirm the consistency of the scanner performance.

MRI scanning protocol

MRI examinations were performed on a 1.5-T scanner (Signa HDxt; GE HealthCare). The protocol included sagittal T1WI (repetition time/echo time, 650/10 ms; section thickness, 4 mm) and STIR images (repetition time/echo time, 3,200/92 ms; inversion time, 150 ms; section thickness, 4 mm) of the thoracic spine.

Postprocessing

The Gemstone Spectral Imaging Viewer was used on the Advantage Workstation 4.7 workstation (GE HealthCare) to analyze the chest spectral CT data files. This software uses two-material decomposition to generate virtual images and obtain corresponding material density values (mg/cm^3).

Standard reference

The MRI images were also independently evaluated by reader 1 and reader 2, who were blinded to relevant clinical and pathological information. The MRI patterns of bone marrow infiltration in MM were assessed and recorded. There are five MRI patterns of bone marrow infiltration in MM (14). In addition to the two patterns of focal infiltration and combined diffuse and focal infiltration, there are three modes of diffuse infiltration, salt-and-pepper infiltration,

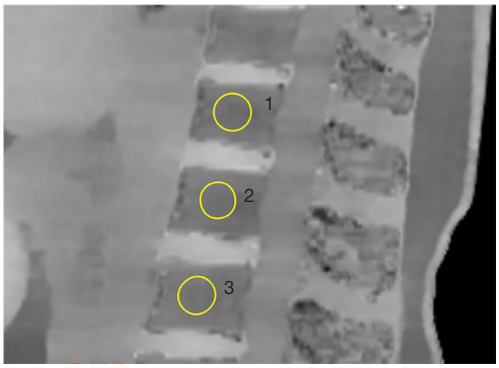

Figure 1 Sketch map of ROIs. Yellow circles 1–3 refer to the ROIs delineated. One of the density materials was chosen for density imaging [i.e., water (HAP), and an ROI of more than 100 mm^2 was drawn on the T11, T12, and L1 vertebrae]. Quantitative data of each ROI were saved. ROIs, regions of interest; HAP, hydroxyapatite.

and normal pattern. Because of the small number of patients with the salt-and-pepper infiltration pattern in this study, we merged them with the diffuse infiltration pattern group. Ultimately, patients with MM were categorized as diffuse infiltration pattern MM (DP-MM) or normal pattern (NP-MM). Disagreements between the readers were resolved by discussion until a consensus was reached.

Region of interest (ROI) delineation

ROIs were delineated by a radiologist with 3 years of experience in musculoskeletal imaging (reader 3) and supervised by another radiologist with 6 years of experience in musculoskeletal imaging (reader 4), with both being blinded to relevant clinical and pathological information. The radiologist browsed images in Gemstone Spectral Imaging viewer mode, and manually drew ROIs of more than 100 mm^2 on the T11, T12, and L1 vertebrae (*Figure 1*) (15). These vertebrae were chosen because abdominal and chest CT scans obtained in clinical practice invariably include them. During delineation of ROIs, care was taken to avoid the basivertebral foramina, bone cortex, bone island, Schmorl's nodule, and hemangioma. For a comparison group, patients with compression fractures in the T11, T12, or L1 vertebrae. If T11, T12, or L1 vertebrae have MRI evidence of edema, adjacent vertebrae (e.g., T10 and L2) would be used.

Quantitative parameter acquisition

The mean CT values of 70-keV images and the basic material density within the ROIs were recorded. In this study, the basic material pairs were the Ca-related pair (Ca-X) and the HAP-related pair (HAP-X), with *X* referring to fat, water, or muscle (MU). Finally, the Ca(X) density and HAP(X) density [$D_{Ca(X)}$ and $D_{HAP(X)}$] were recorded. The average quantitative parameters of the three ROIs of the T11, T12, and L1 vertebrae were used as the final research object.

Statistical analysis

We calculated sample sizes using PASS 21.0 software (NCSS, Kaysville, UT, USA), and the power calculation method was set as a normal approximation. The power and α were set to 0.9 and 0.05, respectively. We assumed that the NOL-MM and comparison groups were the same sizes. With regard to the effect size, we hypothesized that the area under the receiver operating characteristic curve (AUC) would be at least 0.7, and set the input type as proportions. The minimum sample size was calculated to be 82. MedCalc 15.2.2 (MedCalc Software bvba, Ostend, Belgium; http://www.medcalc.org; 2015) was used to compare AUCs, and SPSS 26.0 (IBM Corp., Armonk, NY, USA) was used for other statistical analyses. Continuous variables were compared using the *t*-test or the Mann-Whitney test, and categorical variables were compared using the chi-squared test or Fisher exact test. Material densities with statistically significant differences in concentration were used draw the receiver operating characteristic (ROC) curves of the patients curve and to calculate the AUCs for evaluating the performance of various material densities in diagnosing MM. The cutoff values with the best diagnostic efficacy (i.e., the highest Youden index) were identified, and the sensitivity, specificity, positive predictive value (PPV), negative predictive value (NPV), and accuracy of the diagnosis were calculated. According to the AUC, diagnostic performance was classified as no value (0.5< AUC ≤0.6), poor (0.6< AUC ≤0.7), moderate (0.7< AUC ≤0.8), good (0.8< AUC ≤0.9), and excellent (0.9< AUC ≤1.0) (16). The Delong test was used to evaluate differences between AUCs. Statistical significance was at a two-sided P value <0.05 (17).

Results

A total of 41 consecutive patients with NOL-MM and 41 consecutive healthy patients who showed normal appearance on MRI October 2022 to March 2023 were selected for the study (17 males and 24 females; mean age

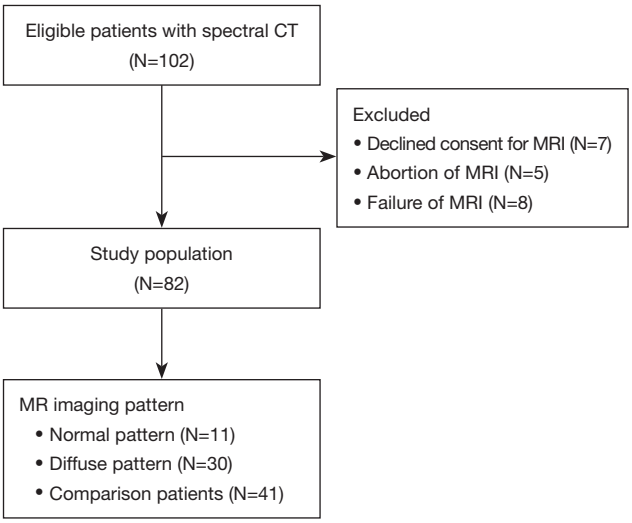

Figure 2 Flowchart showing selection of the study population. Seven patients declined MRI, MRI was aborted in five patients, and MRI failed in eight patients. CT, computed tomography; MRI, magnetic resonance imaging.

57.8 years; age range, 41–80 years) (*Figure 2*). Of the 41 patients with NOL-MM, 30 were categorized as DP-MM and 11 as NP-MM.

Differences in quantitative parameters among different patients

There were no statistically differences in CT values, $D_{HAP(X)}$, or $D_{Ca(X)}$ between the NOL-MM and comparison group, the DP-MM group and comparison group, the NP-MM group and comparison group, or the DP-MM group and NP-MM group (all P values >0.05; *Table 1*).

There were statistically significant differences in $D_{X(HAP)}$ and $D_{X(Ca)}$ between the NOL-MM group and comparison group, the DP-MM group and comparison group, the DP-MM group. NP-MM, and the NP-MM and comparison group (all P values <0.001; *Table 1*).

Performance of CT value, $D_{X(HAP)}$, and $D_{X(Ca)}$ in the diagnosis of NOL-MM

The traditional quantitative CT parameter showed no value for the diagnosis of NOL-MM. For both $D_{X(HAP)}$ and $D_{X(Ca)}$, the diagnostic performance was only related to the virtual removed material and not to the paired material X. $D_{Fat(HAP)}$, $D_{Water(HAP)}$, and $D_{Muscle(HAP)}$ had the same diagnostic performance; $D_{Fat(Ca)}$, $D_{Water(Ca)}$, and $D_{Muscle(Ca)}$ also had the same diagnostic performance (*Tables 2-5*).

$D_{X(HAP)}$ performed better than did $D_{X(Ca)}$ in distinguishing NOL-MM from controls; the diagnostic performance of $D_{X(HAP)}$ was classified as good and that of $D_{X(Ca)}$ as moderate [AUC (95% CI), 0.874 (0.800, 0.949) *vs.* 0.737(0.630, 0.844); P=0.02] (*Table 2*, *Figure 3A*).

$D_{X(HAP)}$ performed better than did $D_{X(Ca)}$ in distinguishing DP-MM from controls; the diagnostic performance of $D_{X(HAP)}$ was classified as excellent and that of $D_{X(Ca)}$ as moderate [AUC (95% CI), 0.933 (0.878, 0.989) *vs.* 0.785 (0.677, 0.894); P=0.01] (*Table 3*, *Figure 3B*).

$D_{X(HAP)}$ performed better than $D_{X(Ca)}$ in distinguishing NP-MM from controls; the diagnostic performance of $D_{X(HAP)}$ was classified as moderate, while $D_{X(Ca)}$ had no value, [AUC (95% CI), 0.714 (0.540, 0.888) *vs.* 0.605 (0.429, 0.782); P=0.03] (*Table 4*, *Figure 3C*).

$D_{X(HAP)}$ performed better than $D_{X(Ca)}$ in distinguishing DP-MM from NP-MM; the diagnostic performance of $D_{X(HAP)}$ was classified as good and that of $D_{X(Ca)}$ as moderate [AUC (95% CI), 0.809 (0.654, 0.964) *vs.* 0.736 (0.566, 0.907); P=0.049] (*Table 5*, *Figure 3D*).

Discussion

This study aimed to evaluate the two-material decomposition technique for detection of bone marrow infiltration in NOL-MM. There were significant differences in both $D_{X(HAP)}$ and $D_{X(Ca)}$ between NOL-MM, DP-MM, NP-MM, and comparison patients. The performance of basic material density in detecting bone marrow infiltration was related to the material removed (i.e., HAP, Ca), but not to the paired material X. $D_{X(HAP)}$ showed better performance than did $D_{X(Ca)}$ for identifying bone marrow infiltration. The optimal cutoff material density values for discrimination of bone marrow infiltration were also determined.

The plasma cells in MM inhibit osteoblasts and enhance osteoclastic activity, leading to decreased bone density and even bone destruction. CT can detect lesions with less than 5% bone trabecular destruction, and so is the first choice for diagnosis of osteolytic bone destruction (18). While CT can accurately identify multiple focal bone destruction caused by focal infiltration of plasma cells, it is not useful for detecting diffuse bone marrow infiltration or nonfocal bone destruction; in these cases, CT may show no significant changes in bone density or only mild decrease in bone density. Meanwhile, severe cases may manifest as osteoporosis indistinguishable from that seen

Table 1 Comparison of basic material density between patients with different types of lesions and control patients

Material	Groups	Density (mg/cm^3)	P
$D_{Fat(HAP)}$	NOL	962.88±15.73	<0.001†
	DP	967.54±13.18	<0.001‡
	NP	950.18±15.58	<0.001§
	CP	939.15±12.32	<0.001¶
$D_{Water(HAP)}$	NOL	1,004.44±16.41	<0.001†
	DP	1,009.29±13.75	<0.001‡
	NP	991.19±16.26	<0.001§
	CP	979.68±12.86	<0.001¶
$D_{MU(HAP)}$	NOL	1,019.18±16.65	<0.001†
	DP	1,024.1±13.96	<0.001‡
	NP	1,005.74±16.51	<0.001§
	CP	994.04±13.05	<0.001¶
$D_{Fat(Ca)}$	NOL	1,019.67±22.13	<0.001†
	DP	1,024.1±22	<0.001‡
	NP	1,007.58±18.3	<0.001§
	CP	1,001.03±18.54	<0.001¶
$D_{Water(Ca)}$	NOL	1,043.34±22.64	<0.001†
	DP	1,047.88±22.51	<0.001‡
	NP	1,030.98±18.74	<0.001§
	CP	1,024.29±18.96	<0.001¶
$D_{MU(Ca)}$	NOL	1,056.01±22.92	<0.001†
	DP	1,060.59±22.79	<0.001‡
	NP	1,043.49±18.96	<0.001§
	CP	1,036.71±19.19	<0.001¶
$D_{HAP(Fat)}$	NOL	123.17±38.74	0.17†
	DP	122.68±40.14	0.19‡
	NP	124.5±36.46	0.90§
	CP	134.26±32.93	0.40¶
$D_{HAP(Water)}$	NOL	82.49±38.83	0.13†
	DP	81.8±40.17	0.15‡
	NP	84.35±36.7	0.86§
	CP	94.58±32.99	0.38¶
$D_{HAP(MU)}$	NOL	77.14±38.86	0.13†
	DP	76.43±40.19	0.14‡
	NP	79.09±36.74	0.85§
	CP	89.37±32.99	0.37¶
$D_{Ca(Fat)}$	NOL	59.08±18.58	0.17†
	DP	58.85±19.25	0.19‡
	NP	59.72±17.49	0.90§
	CP	64.4±15.8	0.40¶
$D_{Ca(Water)}$	NOL	38.81±18.27	0.13†
	DP	38.49±18.89	0.15‡
	NP	39.69±17.27	0.86§
	CP	44.5±15.52	0.38¶
$D_{Ca(MU)}$	NOL	36.21±18.23	0.13†
	DP	35.88±18.86	0.14‡
	NP	37.13±17.23	0.85§
	CP	41.95±15.49	0.37¶

Data are presented as the mean ± standard deviation value of water mass density (mg/cm^3). P values are for the *t*-test; †, NOL-MM *vs.* controls; ‡, DP-MM *vs.* controls; §, NP-MM *vs.* controls; ¶, DP-MM *vs.* NP-MM. HAP, hydroxyapatite; NOL, nonosteolytic; DP, diffuse pattern; NP, normal patter; CP, comparison group; MU, muscle; Ca, calcium; MM, multiple myeloma.

on spinal imaging of non-MM older adults. In the 2003 MM diagnostic criteria, diffuse osteopenia and vertebral compression fracture were considered the defining events of myeloma (19). However, because of the high false-positive rate due to osteoporotic vertebral fractures, these conditions were excluded from the updated 2014 diagnostic criteria (13).

This study found no statistically significant differences in conventional CT values between NOL-MM, NP-MM, DP-MM, and age- and sex-matched controls, indicating the limitations of traditional quantitative diagnostic indicators in the diagnosis of MM. The quantitative parameters $D_{HAP(X)}$ and $D_{Ca(X)}$ of DECT also showed little diagnostic value for MM, indicating that the feasibility of identifying NOL-MM by measuring the content of bone trabeculae is relatively low.

DECT can characterize and distinguish different substances of different atomic number (such as Ca and HAP) by using the energy dependence of X-ray attenuation (3). Most dual-source protocols found in MM studies perform three-material decomposition by subtracting bone mineral components from CT images. The virtual non-Ca images thus obtained have shown good application potential for

Table 2 Diagnostic performance of X(HAP) material density, X(Ca) material density, and CT value in distinguishing NOL-MM from control patients

Parameter	$D_{X(HAP)}$			$D_{X(Ca)}$			CT value
	Fat (HAP)	Water (HAP)	MU (HAP)	Fat (Ca)	Water (Ca)	MU (Ca)	
AUC (95% CI)	0.874 (0.800, 0.949)	0.874 (0.800, 0.949)	0.874 (0.800, 0.949)	0.737 (0.630, 0.844)	0.737 (0.630, 0.844)	0.737 (0.630, 0.844)	0.520 (0.394, 0.646)
P*	<0.001	<0.001	<0.001	<0.001	<0.001	<0.001	0.76
Cutoff	948	989	1,004	1,007	1,030	1,043	123
Sensitivity	0.829	0.829	0.829	0.732	0.732	0.732	0.561
Specificity	0.805	0.805	0.805	0.659	0.659	0.659	0.537
YI	0.634	0.634	0.634	0.391	0.391	0.391	0.098
PPV	0.810	0.810	0.810	0.682	0.682	0.682	0.548
NPV	0.825	0.825	0.825	0.711	0.711	0.711	0.550
Accuracy	0.817	0.817	0.817	0.695	0.695	0.695	0.549

HAP, hydroxyapatite; Ca, calcium; CT, computed tomography; NOL-MM, nonosteolytic multiple myeloma; MU, muscle; AUC, area under the curve; CI, confidence interval; P*, null hypothesis: true area =0.5; YI, Youden index; PPV, positive predictive value; NPV, negative predictive value.

Table 3 Diagnostic performance of X(HAP) material density, X(Ca) material density, and CT value in distinguishing DP-MM from control patients

Parameter	$D_{X(HAP)}$			$D_{X(Ca)}$			CT value
	Fat (HAP)	Water (HAP)	MU (HAP)	Fat (Ca)	Water (Ca)	MU (Ca)	
AUC (95% CI)	0.933 (0.878, 0.989)	0.933 (0.878, 0.989)	0.933 (0.878, 0.989)	0.785 (0.677, 0.894)	0.785 (0.677, 0.894)	0.785 (0.677, 0.894)	0.532 (0.391, 0.672)
P*	<0.001	<0.001	<0.001	<0.001	<0.001	<0.001	0.65
Cutoff	948	989	1,004	1,012	1,035	1,048	130
Sensitivity	0.933	0.933	0.933	0.767	0.767	0.767	0.600
Specificity	0.805	0.805	0.805	0.732	0.732	0.732	0.561
YI	0.738	0.738	0.738	0.498	0.676	0.498	0.500
PPV	0.778	0.778	0.778	0.676	0.811	0.676	0.657
NPV	0.943	0.943	0.943	0.811	0.746	0.811	0.577
Accuracy	0.859	0.859	0.859	0.746	0.767	0.746	0.600

HAP, hydroxyapatite; Ca, calcium; CT, computed tomography; DP-MM, diffuse infiltration pattern multiple myeloma; MU, muscle; AUC, area under the curve; CI, confidence interval; P*, null hypothesis: true area =0.5; YI, Youden index; PPV, positive predictive value; NPV, negative predictive value.

the diagnosis and follow-up of MM (11). Spectral CT can use the two-material decomposition method to remove the X-ray absorption component of bone minerals and thereby obtain a base material concentration unaffected by bone minerals. The decomposition of three materials suggests that virtual decalcification can improve the observation of bone marrow lesions. However, human bones comprise 50% organic matrix (osteoid) and 50% Ca and HAP. Using two-material decomposition to remove HAP may reduce the impact of bone trabeculae on the display of bone marrow

Table 4 Diagnostic performance of X(HAP) material density, X(Ca) material density, and CT value in distinguishing NP-MM from control patients

Parameter	$D_{X(HAP)}$			$D_{X(Ca)}$			CT value
	Fat (HAP)	Water (HAP)	MU (HAP)	Fat (Ca)	Water (Ca)	MU (Ca)	
AUC (95% CI)	0.714 (0.540, 0.888)	0.714 (0.540, 0.888)	0.714 (0.540, 0.888)	0.605 (0.429, 0.782)	0.605 (0.429, 0.782)	0.605 (0.429, 0.782)	0.488 (0.297, 0.679)
P*	0.03	0.03	0.03	0.29	0.29	0.29	0.90
Cutoff	956	998	1,012	1,004	1,027	1,040	108
Sensitivity	0.545	0.545	0.545	0.727	0.727	0.727	0.727
Specificity	0.878	0.878	0.878	0.585	0.585	0.585	0.415
YI	0.423	0.423	0.423	0.312	0.312	0.312	0.142
PPV	0.545	0.545	0.545	0.320	0.320	0.320	0.250
NPV	0.878	0.878	0.878	0.889	0.889	0.889	0.850
Accuracy	0.808	0.808	0.808	0.615	0.615	0.615	0.481

HAP, hydroxyapatite; Ca, calcium; CT, computed tomography; NP-MM, normal pattern multiple myeloma; MU, muscle; AUC, area under the curve; CI, confidence interval; P*, null hypothesis: true area =0.5; YI, Youden index; PPV, positive predictive value; NPV, negative predictive value.

Table 5 The diagnostic performance of X(HAP) material density, X(Ca) material density, and CT value in distinguishing DP-MM from NP-MM

Parameter	$D_{X(HAP)}$			$D_{X(Ca)}$			CT value
	Fat (HAP)	Water (HAP)	MU (HAP)	Fat (Ca)	Water (Ca)	MU (Ca)	
AUC (95% CI)	0.809 (0.654, 0.964)	0.809 (0.654, 0.964)	0.809 (0.654, 0.964)	0.736 (0.566, 0.907)	0.736 (0.566, 0.907)	0.736 (0.566, 0.907)	0.488 (0.375, 0.753)
P*	0.003	0.003	0.003	0.02	0.02	0.02	0.54
Cutoff	964	1,005	1,020	1,014	1,038	1,050	133
Sensitivity	0.667	0.667	0.667	0.700	0.700	0.700	0.600
Specificity	0.909	0.909	0.909	0.818	0.818	0.818	0.727
YI	0.576	0.576	0.576	0.518	0.518	0.518	0.327
PPV	0.952	0.952	0.952	0.913	0.913	0.913	0.857
NPV	0.500	0.500	0.500	0.500	0.500	0.500	0.400
Accuracy	0.732	0.732	0.732	0.732	0.732	0.732	0.634

HAP, hydroxyapatite; Ca, calcium; CT, computed tomography; DP-MM, diffuse infiltration pattern multiple myeloma; NP-MM, normal pattern multiple myeloma; MU, muscle; AUC, area under the curve; CI, confidence interval; P*, null hypothesis: true area =0.5; YI, Youden index; PPV, positive predictive value; NPV, negative predictive value.

lesions. In previous studies, two-material decomposition spectral CT has mainly been used for detecting bone marrow edema or bone metastasis, but there are few reports of its application in MM (20-23). Hu *et al.* compared the performance of $D_{Ca(Water)}$, $D_{Water(Ca)}$, $D_{HAP(Fat)}$, $D_{Fat(HAP)}$, logistic regression models based on $D_{Water(Ca)}$ and $D_{Ca(Water)}$, and logistic regression models based on $D_{Fat(HAP)}$ and $D_{HAP(Fat)}$ for identifying bone marrow infiltration in MM. They found that a single quantitative parameter had limited diagnostic ability, with the exception of $D_{Fat(HAP)}$ (AUC 0.846). The logistic regression model based on $D_{Water(Ca)}$ and $D_{Ca(Water)}$ showed the best performance for distinguishing between

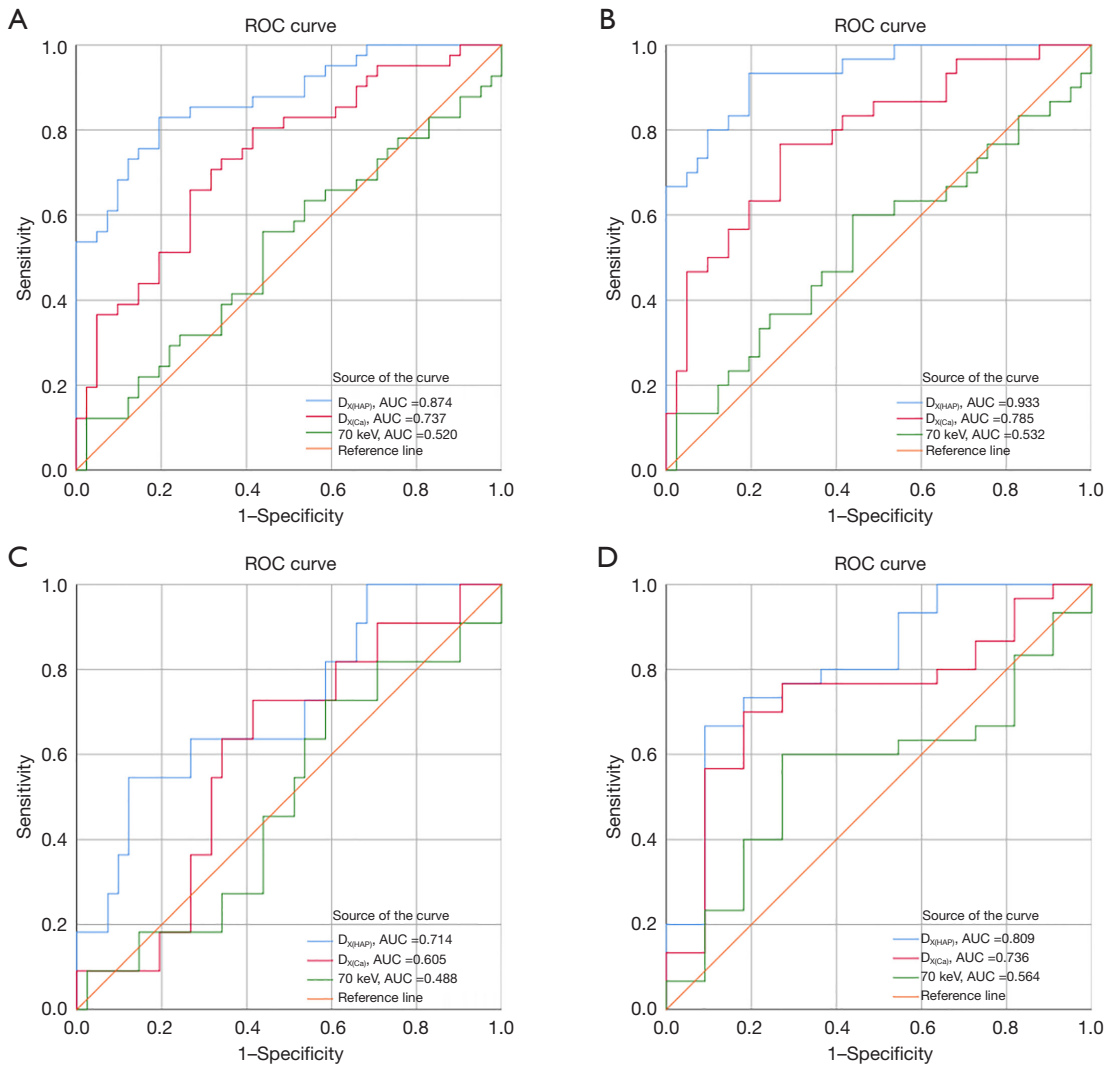

Figure 3 ROC curves of $D_{X(Ca)}$, $D_{X(HAP)}$, and CT values for the diagnosis of MM. (A) ROC curves for differentiation of the NOL-MM group *vs.* the comparison group. (B) ROC curves for differentiation of the DP-MM group *vs.* the comparison group. (C) ROC curves for differentiation of the NP-MM group *vs.* the comparison group. (D) ROC curves for differentiation of the DP-MM group *vs.* NP-MM group. ROC, receiver operating characteristic; HAP, hydroxyapatite; AUC, area under the curve; Ca, calcium; CT, computed tomography; MM, multiple myeloma; NOL, nonosteolytic; DP, diffuse pattern; NP, normal pattern.

infiltration and healthy bone marrow (AUC 0.856) (24). In our study, we did not establish a differential diagnosis model because we found that the density of all basic material pairs showed varying degrees of linear correlation. In a logistic regression model, it is necessary for the respective variables to meet the condition of nonlinear correlation. Hu *et al.* did not elucidate the correlation between $D_{Water(Ca)}$ and $D_{Ca(Water)}$, and therefore their results must be interpreted with caution. In this study, $D_{X(HAP)}$ performed better than did $D_{X(Ca)}$ in the diagnosis of bone marrow infiltration, demonstrating good ability in distinguishing DP-MM patients from controls and NP-MM patients and in as distinguishing NP-MM patients from controls. The moderate-to-excellent performance of $D_{X(HAP)}$ implies that HAP may be closer to the ingredient of bone trabeculae than Ca. Therefore, we recommend removal of the absorption component of HAP in the two-material decomposition to reduce the impact of bone trabeculae on the display of MM bone marrow infiltration lesions.

Many researchers choose to use water or fat paired with

HAP or Ca when analyzing bone lesions on spectral CT. The rationale for this is that these substances are thought to be the main components of bone, and therefore $D_{Water(Ca)}$, $D_{Fat(HAP)}$, or $D_{Ca(X)}$ should be helpful in diagnosing bone-related diseases (21,22,25). In our study, we paired water, fat, and MU with Ca or HAP. We found that regardless of what material X was, as long as it was paired with Ca or HAP, the diagnostic performance of $D_{X(HAP)}$ or $D_{X(Ca)}$ remained consistent; that is, $D_{X(HAP)}$, which has removed the X-ray absorption components of HAP, has good performance in diagnosing NOL-MM. Furthermore, the performance is related to the removed material HAP, but not to the paired material X. This may be explained by the principle of spectral CT. Spectral CT material decomposition is based on the principle that the absorption of any material (CT value) is the sum of the absorption of the other two materials. For example, with X-HAP as the basic material pair, the following equation can be assumed: $\left[\mathrm{CTE} = \mathrm{DX} \times \mu\mathrm{X}(\mathrm{E}) + \mathrm{DHAP} \times \mu\mathrm{HAP}(\mathrm{E})\right]$. CTE indicates the X-ray attenuation for a specific substance (elements, compounds, mixtures, etc.). The μX(E) and μHAP(E) indicate intrinsic X-ray mass attenuation coefficients for X-material and HAP, respectively. DX and DHAP represent the required respective density of X-material and HAP to realize similar X-ray attenuation value of the substance (CTE). From this, we can infer that the absorption component of X-material after removing the influence of HAP is as follows: $\left[\mathrm{DX} \times \mu\mathrm{X}(\mathrm{E}) = \mathrm{CTE} - \mathrm{DHAP} \times \mu\mathrm{HAP}(\mathrm{E})\right]$. Therefore, the result of $\left[\mathrm{DX} \times \mu\mathrm{X}(\mathrm{E})\right]$ is fixed regardless of what X is. Therefore, the X-ray absorption component of the material after HAP removal is most related to NOL-MM.

Our findings also indicated that $D_{X(HAP)}$ could distinguish DP-MM patients from controls and also NP-MM from DP-MM. DP-MM has relatively poor prognosis, so $D_{X(HAP)}$ could be useful for predicting prognosis of patients with MM. $D_{X(HAP)}$ also showed moderate performance in distinguishing NP-MM from comparisons, indicating that it might be useful for screening for plasma cell abnormalities or MM. About 3% of patients aged >50 years have gammaglobulinemia and an attendant 1% risk of developing MM every year. Furthermore, 53.8% of patients with monoclonal gammopathy of undetermined significance have osteopenia, and 26.2% have osteoporosis. Therefore, there is considerable clinical value in being able to distinguish NP-MM patients from non-MM patients (26). However, the discrimination ability of $D_{X(HAP)}$ will have to be confirmed in larger samples, as the number of patients with NP-MM was too small in our study. It should be pointed out that most MM-related studies have small sample sizes, and researchers have generally attempted to overcome this by drawing five ROIs for each patient. In our study, we excluded patients with focal osteolytic bone destruction, and for each NOL-MM, all ROIs should correspond to the same bone marrow infiltration mode, so this type of study should be conducted per patient and not per lesion.

This study has some limitations. First, the sample size was small, and our findings will have to be verified in larger-sample studies. Second, spine data from chest CT were used for analysis, and full-spine CT examination was not performed to avoid additional radiation exposure. In addition, because of the limitation of technology, we only used the most common materials, Ca and HAP, in this study, and change the basis materials to another material that can better mimic the materials present in the body via the basis materials transformation may yield more authentic results. Finally, using HAP as the high-attenuation basis material was superior to Ca in detecting bone marrow infiltration in NOL-MM on spectral CT; however, due to the limitation of equipment conditions in our hospital, we could not compare the performance of two-material and three-material decomposition; therefore, the results may vary across the dual-energy CT scanners of different vendors.

Conclusions

Single-material density images without X-ray absorption components of HAP, obtained using the two-material decomposition technique in spectral CT, appear to have excellent value for diagnosing nonosteolytic bone lesions in patients with MM. The diagnostic performance appears to be related to the removed material HAP but not with its paired material.

Acknowledgments

We thank Elixigen Corporation (Huntington Beach, CA, USA) for helping in proofreading and editing the language of the final manuscript.

Funding: This research was funded by the Talent Start-up Fund Project of Fujian Medical University Union Hospital (Grant No. 2022XH007) and the Fujian Natural Science Foundation (Youth Innovation) (Grant No. 2023J05040).

Footnote

Reporting Checklist: The authors have completed the STARD reporting checklist. Available at https://qims.amegroups.com/article/view/10.21037/qims-23-1042/rc

Conflicts of Interest: All authors have completed the ICMJE uniform disclosure form (available at https://qims.amegroups.com/article/view/10.21037/qims-23-1042/coif). S.C. is employed by GE HealthCare, the manufacturer of the CT scanner used in this study. The other authors have no conflicts of interest to declare.

Ethical Statement: The authors are accountable for all aspects of the work in ensuring that questions related to the accuracy or integrity of any part of the work are appropriately investigated and resolved. This prospective, single-center study was conducted in accordance with the Declaration of Helsinki (as revised in 2013) and was approved by the institutional ethics board of Fujian Medical University Union Hospital. Informed consent was obtained from all participant.

References

1. Treitl KM, Ricke J, Baur-Melnyk A. Whole-body magnetic resonance imaging (WBMRI) versus whole-body computed tomography (WBCT) for myeloma imaging and staging. Skeletal Radiol 2022;51:43-58.
2. Zamagni E, Tacchetti P, Cavo M. Imaging in multiple myeloma: How? When? Blood 2019;133:644-51.
3. Kosmala A, Weng AM, Heidemeier A, Krauss B, Knop S, Bley TA, Petritsch B. Multiple Myeloma and Dual-Energy CT: Diagnostic Accuracy of Virtual Noncalcium Technique for Detection of Bone Marrow Infiltration of the Spine and Pelvis. Radiology 2018;286:205-13.
4. Alvarez RE, Macovski A. Energy-selective reconstructions in X-ray computerized tomography. Phys Med Biol 1976;21:733-44.
5. Stonestrom JP, Alvarez RE, Macovski A. A framework for spectral artifact corrections in x-ray CT. IEEE Trans Biomed Eng 1981;28:128-41.
6. Goh KL, Liew SC, Hasegawa BH. Correction of energy-dependent systematic errors in dual-energy X-ray CT using a basis material coefficients transformation method. IEEE Transactions on Nuclear Science 1997;44:2419-24.
7. Goh KL, Liew SC, Hasegawa BH. Energy-dependent systematic errors in dual-energy X-ray CT. IEEE Transactions on Nuclear Science 1997;44:212-7.
8. Vlahos I, Jacobsen MC, Godoy MC, Stefanidis K, Layman RR. Dual-energy CT in pulmonary vascular disease. Br J Radiol 2022;95:20210699.
9. Boccalini S, Si-Mohamed S, Matzuzzi M, Tillier M, Rotzinger DC, Revel D, Boussel L, Douek P. Effect of contrast material injection protocol on first-pass myocardial perfusion assessed by dual-energy dual-layer computed tomography. Quant Imaging Med Surg 2022;12:3903-16.
10. Marin D, Boll DT, Mileto A, Nelson RC. State of the art: dual-energy CT of the abdomen. Radiology 2014;271:327-42.
11. D'Angelo T, Albrecht MH, Caudo D, Mazziotti S, Vogl TJ, Wichmann JL, Martin S, Yel I, Ascenti G, Koch V, Cicero G, Blandino A, Booz C. Virtual non-calcium dual-energy CT: clinical applications. Eur Radiol Exp 2021;5:38.
12. Cawthray JF, Weekes DM, Sivak O, Creagh AL, Ibrahim F, Iafrate M, Haynes CA, Wasan KM, Orvig C. In vivo study and thermodynamic investigation of two lanthanum complexes, La(dpp)(3) and La(XT), for the treatment of bone resorption disorders. Chem Sci 2015;6:6439-47.
13. Rajkumar SV, Dimopoulos MA, Palumbo A, Blade J, Merlini G, Mateos MV, et al. International Myeloma Working Group updated criteria for the diagnosis of multiple myeloma. Lancet Oncol 2014;15:e538-48.
14. Dimopoulos MA, Hillengass J, Usmani S, Zamagni E, Lentzsch S, Davies FE, et al. Role of magnetic resonance imaging in the management of patients with multiple myeloma: a consensus statement. J Clin Oncol 2015;33:657-64.
15. Ma Q, Hou X, Cheng X, You Y, Yang Z, Ma D, Wang Z. Risk of vertebral fractures: evaluation on vertebral trabecular attenuation value and hydroxyapatite concentration in patients by chest spectral CT. Br J Radiol 2021;94:20200234.
16. Chang E, Tian Y, Wang C, Deng N, Jiang Z, Liu C. Exploring the Phylogeography of Ancient Platycladus

orientalis in China by Specific-Locus Amplified Fragment Sequencing. Int J Mol Sci 2019;20:3871.
17. Points of significance. Nat Hum Behav 2023;7:293-4.
18. Chrzan R, Jurczyszyn A, Urbanik A. Whole-Body Low-Dose Computed Tomography (WBLDCT) in Assessment of Patients with Multiple Myeloma - Pilot Study and Standard Imaging Protocol Suggestion. Pol J Radiol 2017;82:356-63.
19. Criteria for the classification of monoclonal gammopathies, multiple myeloma and related disorders: a report of the International Myeloma Working Group. Br J Haematol 2003;121:749-57.
20. Ishiwata Y, Hieda Y, Kaki S, Aso S, Horie K, Kobayashi Y, Nakamura M, Yamada K, Yamashiro T, Utsunomiya D. Improved Diagnostic Accuracy of Bone Metastasis Detection by Water-HAP Associated to Non-contrast CT. Diagnostics (Basel) 2020.
21. Son W, Park C, Jeong HS, Song YS, Lee IS. Bone marrow edema in non-traumatic hip: high accuracy of dual-energy CT with water-hydroxyapatite decomposition imaging. Eur Radiol 2020;30:2191-8.
22. Pan J, Yan L, Gao H, He Y, Zhong Z, Li P, Zhang Y, Guo Y, Liao L, Zhou S, Zhang K. Fast kilovoltage (KV)-switching dual-energy computed tomography hydroxyapatite (HAP)-water decomposition technique for identifying bone marrow edema in vertebral compression fractures. Quant Imaging Med Surg 2020;10:604-11.
23. Luo S, Guan X, Zhang Y, Zhang X, Wan Y, Deng X, Fu F. Quantitative evaluation of bone marrow characteristics in occult and subtle rib fractures by spectral CT. Jpn J Radiol 2023;41:1117-26.
24. Hu C, Zhang Y, Xiong X, Meng Q, Yao F, Ye A, Hao Z. Quantitative evaluation of bone marrow infiltration using dual-energy spectral computed tomography in patients with multiple myeloma. J Xray Sci Technol 2021;29:463-75.
25. Xie C, Ather S, Mansour R, Gleeson F, Chowdhury R. Dual-energy CT in the diagnosis of occult acute scaphoid injury: a direct comparison with MRI. Eur Radiol 2021;31:3610-5.
26. Zamagni E, Nanni C, Gay F, Pezzi A, Patriarca F, Bellò M, et al. 18F-FDG PET/CT focal, but not osteolytic, lesions predict the progression of smoldering myeloma to active disease. Leukemia 2016;30:417-22.

Cite this article as: Chen J, Qiu Z, Jiang N, Xia Y, Li H, Chen S, Liu J, Xue Y. Detecting bone marrow infiltration in nonosteolytic multiple myeloma through separation of hydroxyapatite via the two-material decomposition technique in spectral computed tomography. Quant Imaging Med Surg 2024;14(3):2345-2356. doi: 10.21037/qims-23-1042

